Journal of Materials Chemistry A

ROYAL SOCIETY OF CHEMISTRY

PAPER

View Article Online
View Journal | View Issue

Open Access Article. Published on 21 August 2025. Downloaded on 3/5/2026 6:20:05 PM.
This article is licensed under a Creative Commons Attribution-NonCommercial 3.0 Unported Licence.

Check for updates

Cite this: J. Mater. Chem. A, 2025, 13, 32815

Simultaneous shaping and reduction of binder-free electrochemically reduced graphene oxide electrodes through cathodic electrophoretic deposition (EPD)

Oxel Urra Sanchez, *[ac] Joaquin Yus, [ab] Antonio Javier Sanchez-Herencia [a] and Begoña Ferrari [a]

Received 3rd February 2025
Accepted 19th August 2025

DOI: 10.1039/d5ta00888c

rsc.li/materials-a

It is well known that the exposed specific surface governs the electrochemical performance of capacitive materials. In this context, the predominant strategy involves using sustainable 2D nanoparticles with a high specific surface area, with graphene being the most explored. The electrochemical behaviour of the material always depends on its intrinsic properties, but the processing route is a critical aspect to consider when it comes to exploiting the full inherent capability of the material to obtain high-performance supercapacitor electrodes. The configuration and arrangement of the formed microstructure are crucial for maximizing the electrochemically active sites of the material. This work presents an innovative colloidal approach for the cathodic electrophoretic deposition (EPD) of graphene oxide (GO). By modifying the GO surface with a cationic polyelectrolyte (polyethylene imine, PEI), the electrophoretic movement and deposition on the cathode are promoted. During the deposition process, the π electronic network of the GO is partially restored and the electronic properties of the substrate/coating interface are enhanced by the adjustment of the electrokinetic and suspension parameters. Results indicate an increase of 20% in the electrochemically active surface area (ECSA) for the same quantity of deposited electroactive material. This is a consequence of the more compact and active microstructures created over the 3D metallic substrates, following the electrically driven colloidal approach. The electrochemical characterization of the electrodes developed herein was compared with that of other reported ErGO electrodes, displaying a competitive supercapacitor behaviour with a specific capacity ranging from 148 to 80 F g^{-1} (1.5–4.0 A g^{-1}), retention of 62%, and a power density of 1.1×10^3 W Kg^{-1}.

Introduction

As renewable sources become a central component of global energy production, the development of a new worldwide energy network is required. New devices capable of storing large energy densities and high-power densities simultaneously with high charge–discharge velocities are needed.[1] Supercapacitors (SCs) have attracted special attention as they can achieve rapid charge–discharge capacities while providing larger energy densities at high current densities with excellent cycling stability.

According to the literature, depending upon the energy storage mechanism, three different types of SCs can be found.[2] The electrochemical double-layer capacitors (EDLCs) have an energy storage mechanism based on the formation of an electrochemical double-layer due to the electrostatic forces and fast ion adsorption/desorption processes. Due to their high dependence on active surface area, EDLCs are mostly based on porous 2D materials, where the high specific surface area provides high capacitance values in comparison to electrostatic capacitors. High-performance EDLC electrodes are governed mainly by carbon materials, where the 3D carbon networks have emerged as exceptionally promising materials for constructing supercapacitor electrodes. This is attributable to their sustainable sources, excellent electronic conductivity, high specific surface area, hierarchical porous structures, and physicochemical stability. The surface morphology of carbon materials is a key factor in the performance of the electroactive material.[3]

Among the different materials within the carbon family, graphene is a renowned two-dimensional material with strong mechanical strength (~1 TPa), high electrical and thermal conductivity, and a highly modifiable specific surface area (up

[a]Tailoring Throug Colloidal Processing Group, Instituto de Ceramica y Vidrio (ICV), CSIC, Calle Kelsen 5, 28049, Madrid, Spain. . E-mail: oxel@icv.csic.es

[b]University of Illinois at Urbana-Champaign, 1206 W Gregory Dr, Urbana, IL 61801, USA

[c]Escuela de doctorado, Universidad Autónoma de Madrid, 28049 Madrid, Spain

Open Access Article. Published on 21 August 2025. Downloaded on 3/5/2026 6:20:05 PM.
This article is licensed under a Creative Commons Attribution-NonCommercial 3.0 Unported Licence.

to 2675 m^2 g^{-1}).[4–7] Graphene oxides (GO) may appear with different functional groups (hydroxyl (C–OH), carboxyl (C=O), and epoxy groups (C–O)) and different oxidation ranges depending on the exfoliation process. Oxygen functional groups improve the carbon surface's wettability, enabling the ionization or chemical modification of the surface to obtain a well-dispersed and stabilized suspension. The presence of oxygen functional groups disrupts the π electron cloud, reducing the electrical conductivity of graphene, as well as leading to a polarization effect at high voltages during the charge–discharge processes, provoking rapid capacity loss at high current rates.[16,17]

Thus, reducing GO to obtain reduced graphene oxide (rGO) is a low-cost strategy commonly used to maximize the electrochemical properties of the active material. rGO presents greater electrochemical properties with higher electrical conductivity and larger specific capacitance values than GO. Different strategies, such as chemical reduction, thermal reduction, and catalytic reduction, have been explored to reduce GO.[18–20] However, these aggressive graphene oxide reduction routes have been proven to cause a major increase in defects in the atomic structure and electronic network of graphene, decreasing its electrical properties.[21] In addition, the need for toxic agents and long chemical or thermal treatments highlights the necessity for developing more sustainable pathways. In this sense, electrochemical reduction has been established as one of the most effective methods for generating environmentally sustainable, high-performance electrodes on a large scale for EDLCs.[22]

Electrophoretic deposition (EPD) is extensively utilized across diverse industrial sectors for the large-scale production of 2D monolithic thin deposition due to its versatility, efficiency, and rapid processing times.[23,24] EPD of different carbonaceous materials, including carbon nanotubes (CNT), graphene oxide (GO), different graphene-containing nanocomposites, such as graphene-NiO, graphene-TiO, rGO-MnO_2, and combinations of graphene with polymers, were recently developed.[25,26] Most of the studies focused on improving the mechanical and chemical properties in the deposited substrates, taking advantage of the shaping freedom offered by EPD to form compact films.[27–29] Nevertheless, while EPD is a well-established technique for scalable and eco-friendly processing of GO, most prior studies rely on anodic EPD, which necessitates a subsequent electrochemical reduction step to enhance the properties of the GO flakes. Table 1 displays distinct strategies for the reduction and shaping of GO to fabricate EDLC electrodes, alongside their electrochemical performance.

Numerous strategies have been reported for the fabrication of reduced rGO and electrochemically reduced graphene oxide (ErGO) coatings. Recently, Srinivas Gadipelli *et al.*[8] reported exfoliated and thermally reduced rGO electrodes prepared using three distinct shaping techniques across various substrates. Notably, the electrodes formed by the direct pressing of dry powders onto nickel foam exhibited a high specific capacitance of 340 F g^{-1} at 0.5 A g^{-1} in 1 M KOH using a three-electrode configuration. Alternatively, Wnali *et al.*[9] employed a dip-coating technique to deposit GO onto gold electrodes, followed by electrochemical reduction to produce ErGO films. Previous studies have shown that reducing oxygen-containing groups in GO improves its viscoelasticity and charge storage, reaching 160.8 F g^{-1} *via* cyclic voltammetry (CV). Other authors used a chronoamperometry technique applying a potential difference of −1 V for 5 minutes and 2 h to generate a GO coating.[11,12] Cu wire substrates with hydrazine-based chemical reduction yielded 117.5 F g^{-1} (ref. 11) while Xuejun *et al.* reported 126.4 F g^{-1} through simultaneous electrophoretic deposition and electrochemical reduction in 1 M Na_2SO_4.[12]

Table 1 Overview of the electrically driven deposition, reduction, and electrochemical performance of rGO electrodes. Specific capacitance (C_s); energy density (E); power density (P); and electrochemical reduction (ECr)

Precursor material	Shaping configuration	GO reduction mechanism	C_s F g^{-1}	E (Wh kg^{-1})	P (W kg^{-1})	Electrochemical characterization conditions	Ref.
Exfoliated GO	Drop-casting	Thermal reduction	340.0	—	—	0.5 A g^{-1}; −0.8 V to 0 V 1 M KOH	8
GO	Dip-coating	ECr in 0.5 M $NaNO_3$	160.8	—	—	10 mV s^{-1}; −0.5 V to 0.5 V 1 M NaCl	9
GO	2 electrode EPD	ECr in H_3PO_4	81.0	11.2	250	0.5 A g^{-1}; 0 V to 1 V PVA-1 M H_3PO_4	10
GO	3 electrode EPD	Chemical reduction	117.5	10.4[a]	520[a]	0.5 A g^{-1}; 0 V to 0.8 V PVA-H_3PO_4	11
GO	3 electrode EPD	ECr in 1 M Na_2SO_4	126.4	17.5[a]	1715[a]	0.5 mA cm^{-2}; −1 V to 0 V 1 M Na_2SO_4	12
rGO	2 electrode EPD	Chemical reduction	142.0	19.7[a]	236[a]	0.2 A g^{-1}; 0 V to 1 V PVA-H_3PO_4	13
GO	2 electrode EPD	Chemical reduction	195.0	27.1[a]	271[a]	0.5 A g^{-1}; −1 V to 0 V 6 M KOH	14
GO varying concentration	3 electrode EPD	ECr in 0.5 M NaCl varying potential differences	167.0	15.1	247	0.5 A g^{-1}; −0.2 V to 0.8 V 0.5 M H_2SO_4	15

[a] Calculated values using the given C_s data and eqn (10) and (11).

Open Access Article. Published on 21 August 2025. Downloaded on 3/5/2026 6:20:05 PM. This article is licensed under a Creative Commons Attribution-NonCommercial 3.0 Unported Licence.

Baozhen *et al.*[15] deposited GO on biochar using a three-electrode setup (3 V *vs.* SCE, 10 min) with suspension concentrations of 0.05–2 g L^{-1}, achieving up to 167 F g^{-1} by tuning the GO content and reduction conditions. A two-electrode setup was used by Purkait *et al.*[10] to coat a Cu wire, reaching 81 F g^{-1} in PVA/H_3PO_4-based flexible supercapacitors. Wang *et al.* and Zisong *et al.* employed similar systems with stainless steel and nickel foam using hydrazine reduction either before (142 F g^{-1}) or after (195 F g^{-1}) deposition.[13]

The reduction of oxygen groups restores the π-network, enabling fast charge–discharge cycles and boosting power densities (200–1800 W kg^{-1}), while energy densities remain around 10–30 Wh kg^{-1}. However, these approaches rely on anodic GO deposition and require separate chemical or electrochemical reduction steps in salt-rich or acidic media, hindering scalability and sustainability.

In this work, we propose a novel, eco-friendly colloidal strategy for the simultaneous shaping and cathodic reduction of compact, binder-free ErGO coatings *via* cathodic EPD in water-based media. A one-step surface modification approach was developed to achieve colloidal stabilization and functionalization of GO, enabling its direct cathodic deposition and *in situ* reduction, eliminating the need for post-treatment steps. By tuning the colloidal and electrokinetic parameters, both deposition and reduction processes were precisely controlled, yielding cohesive ErGO coatings with tunable thicknesses to minimize fracture or delamination.

The resulting compact microstructures were deposited on various Ni-based substrates to demonstrate the versatility and robustness of the method. This approach allows for the fabrication of shaped, binder-free electrodes with optimized microstructural integrity and electrochemical properties. By enhancing the intrinsic conductivity of the reduced carbon network and improving the electrode architecture, the electrochemically active surface area (ECSA) was significantly increased. As a result, the symmetric supercapacitor exhibited enhanced performance, achieving high power densities through a sustainable, low-cost, and scalable single-step processing route.

Experimental

The quantity of polyelectrolyte for the effective surface modification of commercial graphene oxide powder (GO, Graphene-Tech, Spain) was determined by laser Doppler velocimetry using a Zetasizer Nano ZS (Malvern Instruments Ltd, UK) as described elsewhere.[30] Zeta potential determination of PEI-GO nanoflakes was made using concentrations of 0.1 g L^{-1} with 10^{-2} M KCl as the solvent and inert electrolyte to maintain the ionic strength of the suspension medium. The electrokinetic behaviour of modified PEI-GO at different pH levels was evaluated by adding small aliquots of HNO_3 and TMAH controlled with a pH probe (Metrohm AG, Germany).

After surface modification, PEI-GO nanoflakes were centrifuged and cleaned twice with ethanol to remove the remaining ions and the excess stabilizer. The as-centrifuged inorganic particles were re-suspended in an ethanol/water solution (19 : 1), a previously validated EPD medium, to obtain a 1 g L^{-1} suspension.[31] Subsequently, cathodic EPD was carried out over Ni plate/foam (Nickel plate/foam 99%, Goodfellow, UK) substrates following the conditions summarized in Table 2. No further cleaning processes were performed after cathodic EPD.

Table 2 EPD conditions

Substrate	Ni plate/Ni foam
Substrate area[a]	1.5 cm^2
Suspension volume	30 mL
Distance between electrodes	2 cm
Counter electrode	Platine foil
Suspension concentration	1 g L^{-1} PEI-GO in EtOH : H_2O 19 : 1

[a] Geometrical area of the substrates.

The experimental cathodic EPD electrical parameters and kinetic curves were determined under galvanostatic conditions using a high voltage power source (2611 System SourceMeter, Keithley Instruments Inc., USA), applying current densities from 20 to 53 μA cm^{-2} with electric field values from 53 to 135 V cm^{-1}, at deposition times of 0 to 600 seconds.

Theoretical kinetics were determined using the model proposed by Sarkar and Nicholson:[32]

$$m = m_0(1 - e^{-t/\tau}) \tag{1}$$

$$\tau = \frac{V}{f \times \mu_e \times S_D \times E} \tag{2}$$

$$E = \frac{I}{\sigma \times S_C} \tag{3}$$

where m is the deposited mass (g), m_0 is the total mass in the suspension (g), t is the time (s), V is the volume (ml), f is the sticking factor, μ_e is the electrophoretic mobility (cm^2 V^{-1} s^{-1}), S_D is the deposition surface (cm^2), E is the applied electric field (V cm^{-1}), σ is the conductivity of the suspension (mS cm^{-1}) and S_C the conducting area (cm^2), being $S_C = S_D/2$, neglecting the influence of the substrate back face on the applied electric field during the deposition process. After the optimization of the EPD process, the electrodes (substrate + PEI-GO-based electrochemically active coating) were treated thermally at 300 °C for 2 h under argon atmosphere, with heating and cooling rates of 4 °C min^{-1} to strengthen the film microstructure and improve the carbon/nickel interface. The same process was carried out with 0.5 g L^{-1} and 0.1 g L^{-1} PEI-GO nanoflake suspensions, as well as using the Ni foams as substrates to prepare electrodes with optimized homogeneous depositions. XRD characterization was performed using a D8 Advance Bruker X-ray diffractometer with Cu Kα radiation (λ = 1.5418 Å) at 40 KV, 30 mA, and 2θ = 10–70. The morphology and atomic structure of the graphene coatings were analysed by Raman spectroscopy performed on a spectrometer (In *Via* Renishaw plc., UK) with an excitation wavelength of 514 nm produced by an Ar^+ laser.

The coating surface was examined using X-ray photoelectron spectroscopy (XPS) analyses on an ultra-high vacuum Thermo-Fisher Scientific K-Alpha X-ray photoelectron spectrometer

Open Access Article. Published on 21 August 2025. Downloaded on 3/5/2026 6:20:05 PM. This article is licensed under a Creative Commons Attribution-NonCommercial 3.0 Unported Licence.

system, equipped with a hemispherical energy analyzer and a monochromatic X-ray source was used for surveying the photoemission spectra.

The N_2 adsorption/desorption isotherms and BET specific surface area (SSA) determination for GO nanoflakes were carried out with an accelerated surface area and porosimetry system (ASAP 2020, Micromeritics Instrument Corp., Atlanta, GA, USA). The nanoflake coating and the morphology of the shaped nanostructures were observed with a field emission scanning electron microscope (FESEM, Hitachi S4700, Japan).

Electrochemical characterization was first carried out in a three-cell configuration with a Potentiostat/Galvanostat Autolab (PGSTAT302N, Switzerland). The fabricated working electrodes were directly tested after thermal treatment. The employed electrolyte was a 1 M KOH aqueous solution, while the reference electrode was Ag/AgCl and the counter electrode was Pt foil. Cyclic Voltammetry (CV) was executed in five sequential cycles at a scan rate ranging from 2–100 m V s^{-1} in a potential window of −0.8 to 0 V. The specific capacitance was determined in gravimetric terms (F g^{-1}) from the galvanostatic charge–discharge analysis (GCD) at different current densities (1.5 A g^{-1}, 2 A g^{-1}, 2.5 A g^{-1}, 3 A g^{-1}, 3.5 A g^{-1}, 4 A g^{-1}) in the potential window of the carbonaceous species (−0.6 to 0 V).

Thus, the specific gravimetric capacitance (C_S) was obtained from the following equation:

$$C_S = \frac{I \times \Delta t}{m \times \Delta V} \tag{4}$$

where C_S (F g^{-1}) is the specific capacitance, I (A) is the discharge current, Δt (s) is the discharge time, ΔV (v) is the voltage window for discharge, and m (g) is the mass of the exposed coating.

Additionally, the electrochemically active surface area (ECSA) was calculated by the differential capacitance measurement (DCM) approach using different cyclic voltammetry measurements at different scan rates in the potential range previously set. The measurement is made in the non-faradaic reaction region of the electrode, resulting in differential capacitance equivalent to the double layer capacitance (C_{DL}). Knowing the theoretical specific areal capacitance (C_{TS}) value for the GO surface area, which defines the capacitance of an ideal flat surface on the formation of the electrochemical double layer, the electrochemically active surface area was calculated using the following equation:[33]

$$\text{ECSA} = \frac{C_{DL}}{C_{TS}} \tag{5}$$

The theoretical specific areal capacitance C_{TS} (μF cm^{-2}) is determined by the value of 21 μF cm^{-2}, which was reported in the literature as the specific capacitance of a single-layer graphene oxide, and double-layer capacitance (C_{DL}) is calculated using the following equations:[34]

$$C_{DL} = \frac{dQ}{d\varphi}, \quad i = \frac{dQ}{dQ(\varphi)} \tag{6}$$

where Q (C) is the charge and φ (V) is the potential. From these two eqn (5) and (6), the consecutive equation is derived:

$$i = C_{DL}\frac{d\varphi}{dt} \tag{7}$$

By plotting the current values i (A) of a specific potential value as a function of different scan rates (V s^{-1}), we can obtain a linear behaviour curve, where the slope will give us the double-layer capacitance values.

The resulting ECSA values were compared with the deposited BET area (cm^{-2}) of commercial graphene oxide to calculate the efficiency of the shaping method and calculate the percentage of the active deposited graphene oxide mass, using the following equations.

$$\text{Deposited BET area} = S_{BET} \times \text{deposited mass} \tag{8}$$

$$\text{Active material}(\%) = \frac{\text{ECSA}}{\text{Deposited BET area}} \times 100 \tag{9}$$

Electrochemical impedance spectroscopy (EIS) measurements were performed in a potentiostatic mode at ambient temperature in the frequency range of 0.1–10^6 Hz with an applied voltage of 50 mV.

Further, (E) energy (Wh kg^{-1}) and (P) power (W kg^{-1}) densities were calculated in a symmetric full-cell configuration in 1 M KOH electrolyte using eqn (10) and (11), respectively:

$$E = \frac{1}{2}C_S U^2 \frac{1000}{3600} \tag{10}$$

$$P = \frac{E}{\Delta t} \tag{11}$$

where C_S represents the measured specific gravimetric capacitance (F g^{-1}), U is the applied cell voltage (V), and Δt is the discharge time (s).

Results and discussion

As graphene is a 2D material, textural properties and the exposed specific surface area are of greater importance when analysing the stabilization of the particles for their processing as catalytic or electrochemically active materials. Thus, the specific surface area and the porosity of the raw material were first determined by N_2 adsorption/desorption measurements. Fig. 1 shows the adsorption isotherm (a) and pore size distribution (b).

The N_2 adsorption/desorption curve exhibits an IV isotherm shape and hysteresis H3 type loop above $P{\cdot}P_0^{-1} > 0.4$. The isotherms of as-received GO were evaluated to confirm the existence of micropores and mesopores. The powders exhibited significant adsorption of N_2 below the relative pressure ($P{\cdot}P_0^{-1}$) of 0.1, indicating the presence of micropores. The pore size distribution derived from the N_2 adsorption isotherm using the BJH model is plotted in Fig. 1(b), confirming the presence of micropores with a diameter ranging from 2 to 4 nm. The morphological and textural parameters are given in Table 3.

A considerable specific surface area of 481.7 m^2 g^{-1} is divided into micropores and others, being 112.6 to 369.2 m^2 g^{-1} respectively, representing the micropore volume of only 8%

Open Access Article. Published on 21 August 2025. Downloaded on 3/5/2026 6:20:05 PM.
This article is licensed under a Creative Commons Attribution-NonCommercial 3.0 Unported Licence.

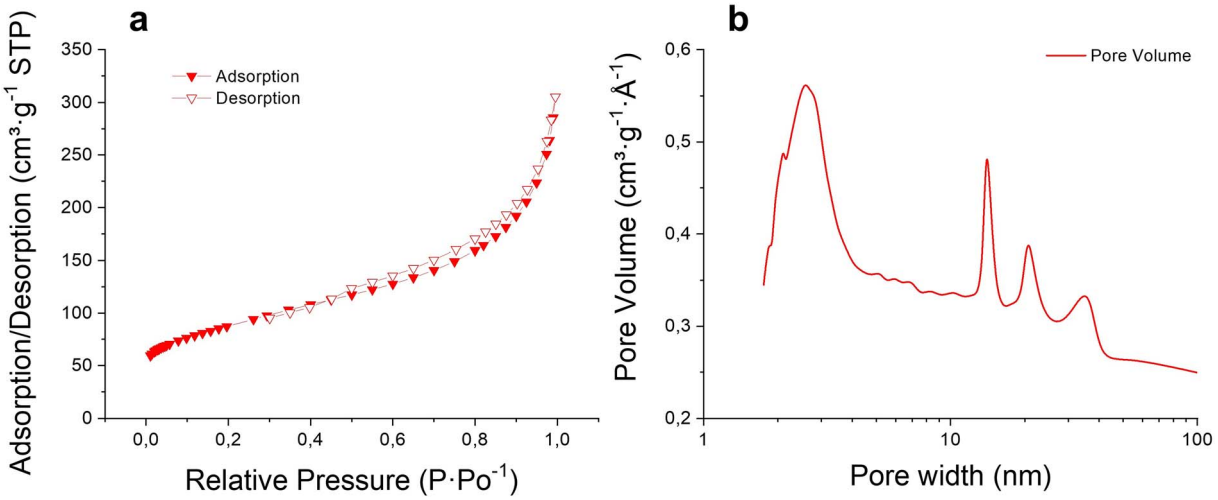

Fig. 1 N_2 adsorption/desorption isotherm curves of graphene (a) and accelerated surface area and microporosimetry (ASAP) analysis curves (b).

Table 3 Textural properties of the as-received GO powders, including surface areas and pore volumes

Mesoporous isotherm	
$^{a}S_{BET}$ (m^2 g^{-1})	481.7
$S_{external}$ (m^2 g^{-1})	369.2
$^{b}S_{micro}$ (m^2 g^{-1})	112.6 (23.4%)
$^{c}V_{Total}$ (cm^3 g^{-1})	0.62
$V_{external}$ (cm^3 g^{-1})	0.57
$^{d}V_{micro}$ (cm^3 g^{-1})	0.05 (8.2%)

[a] Brunauer–Emmett–Teller surface area calculated in the pressure range ($P{\cdot}P_0^{-1}$) of 0.01–0.12. [b] Micropore surface areas calculated from the N_2 adsorption isotherms using the *t*-plot method. [c] Total pore volume obtained at 0.99 of $P{\cdot}P_0^{-1}$. [d] Micropore volume calculated using the *t*-plot method.

(0.05 cm^3 g^{-1}) of the total pore volume of the powder (0.62 cm^3 g^{-1}). Previously reported results showed that the as-received GO powders are composed of around 10 stacked GO nanoflakes, while colloidal characterization revealed structural defects, mainly oxygen-containing functional groups, such as hydroxyl or carboxyl.[30] Consequently, nanoflake stacking could be the cause of the large open porosity of the as-received powders while microporosity could be attributed to the rough and defective structure of the own nanoflake.

The effective PEI quantity for the colloidal stabilization of the GO nanoflakes was previously analyzed elsewhere.[30] By adding different percentages of the polyelectrolyte and determining the zeta potential in an inert electrolyte, completely colloidally stabilized GO nanoflakes were obtained when adding 4 wt% of PEI, referred to as the solid content. To ensure the effective colloidal stabilization during cathodic EPD performance in the selected ethanol/water solution (19 : 1) medium,[31] Fig. 2(a) shows the zeta potential evolution with the PEI-GO modified and bare GO nanoflakes at different pH. The bare GO exhibits a positively charged surface below pH 4 while turning negative over pH 5. The adsorbed PEI on the GO nanoflake surface switches to a positively charged PEI-GO nanoflake for almost all the pH range. The amine functional groups of the branched polyelectrolyte display a protonated behaviour up to pH 9, maintaining over 50 mV at pH 8.

Fig. 2(c) displays a scheme of the flocculation process of PEI-GO nanoflakes when they deposit in the cathodic electrode during electrophoresis. At the cathode surroundings, the evolution of H_2 and the consequent reduction of the proton concentration generates an increase in pH, provoking the deprotonation and neutralization of the PEI branched chains. Thus, the modified nanoflakes flocculate while the particle concentration increases, improving packing and leading to the formation of a cohesive coating on the substrate surface.

The kinetics, applying different current densities of 20, 40 and 53 μA cm^2 with electric fields of 53, 81 and 135 V cm^{-1}, respectively, were evaluated in the 19ETOH : 1H_2O medium[31] to obtain the most homogeneous compacted coating while maximizing the electrochemically active exposed surface area (Fig. 2(b)). The evolution of the experimental deposition process at different deposition times ranging from 60 to 600 s is compared with the theoretical approach of the kinetics of PEI-GO nanoflakes, calculated using the electrokinetic parameters summarised in Table 4 and kinetic eqn (1)–(3). The theoretical deposition yield was estimated considering the characteristic time (τ), which depends on the applied current (I), suspension conductivity (σ), and electrophoretic mobility (μ_e). Solid lines represent the theoretical deposition while dotted lines show the evolution of the experimental data.

For the two lowest current densities (20 μA cm^{-2} and 40 μA cm^{-2}), the experimental data suit the theoretical prediction for almost all the range of deposition time tested. However, when the current density is increased (53 μA cm^{-2}), the deposition process steps up. The experimental deposited mass exceeds the expected results from the theoretical approach for all the recorded times, probably due to the synergic effect of the fast electrophoresis and simultaneous flocculation. Therefore, 53 μA cm^{-2} was set as a working current to determine the coating evolution.

Open Access Article. Published on 21 August 2025. Downloaded on 3/5/2026 6:20:05 PM.
This article is licensed under a Creative Commons Attribution-NonCommercial 3.0 Unported Licence.

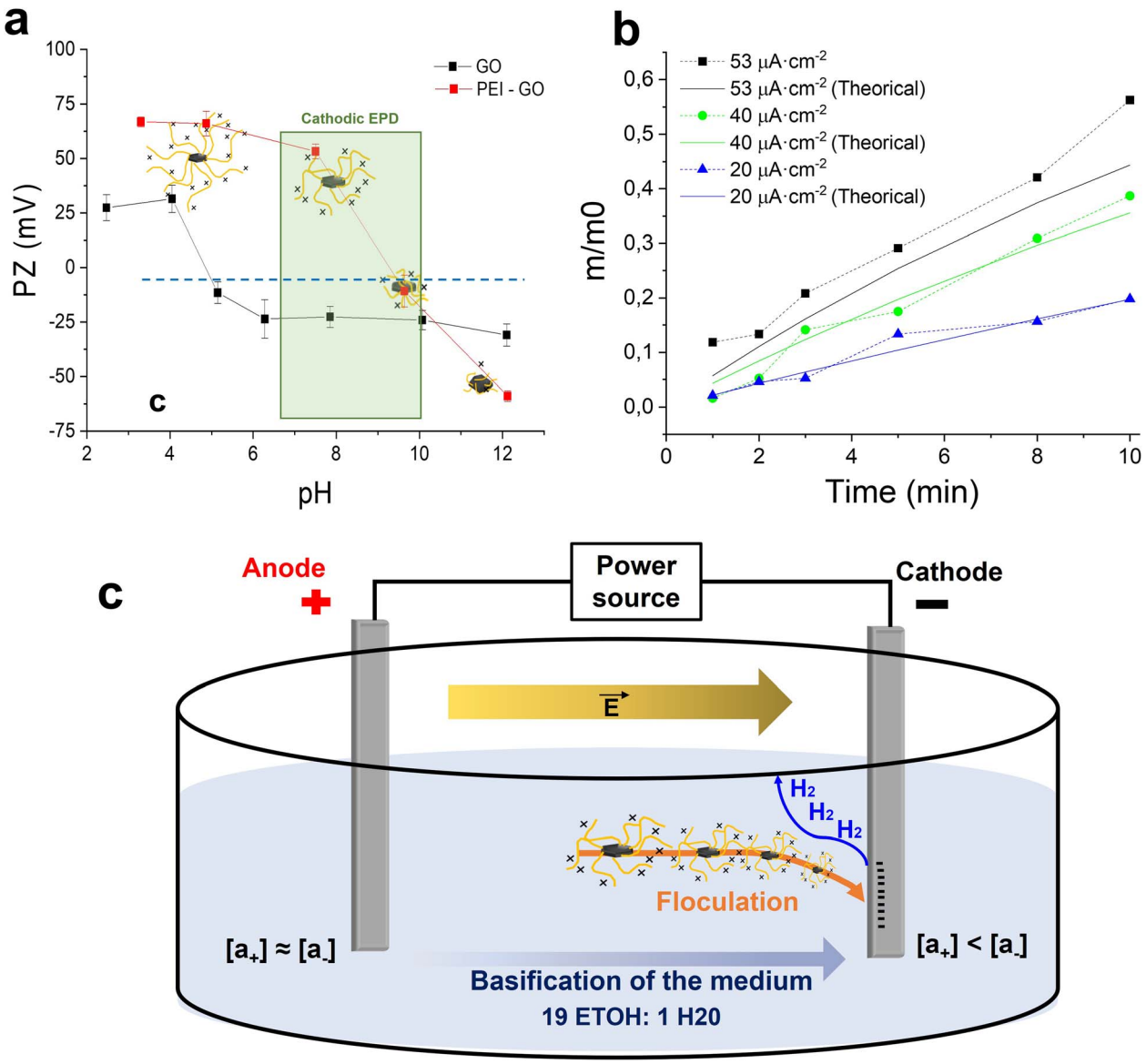

Fig. 2 (a) Evolution of the zeta potential of GO and PEI-GO as function of pH. (b) Experimental (dotted line) and theorical (solid line) electrophoretic deposition kinetics using 1 g L^{-2} suspension of PEI-GO and different current densities (53 μA cm^{-2}, 40 μA cm^{-2}, and 20 μA cm^{-2}). (c) Scheme of the flocculation and deposition process of PEI-GO during the cathodic EPD.

Table 4 Starting conditions of the suspension for the theoretical approximation of EPD

Parameters defining the EPD conditions			
Electrophoretic mobility, μ_e	1.17×10^{-3} cm^2 V^{-1} s^{-1}		
Conductivity, ⌈	3.2×10^{-6} S cm^{-1}		
Initial current density, I cm^{-2}	20 μA cm^{-2}	40 μA cm^{-2}	53 μA cm^{-2}
Deposition time, t	60–600 s	60–600 s	60–600 s
Characteristic time for EPD[a], τ (eqn (2))	2729 s	1365 s	1023 s

[a] Calculated for a volume of suspension of 30 mL (1 g L^{-1}), sticking factor of 1 and an arbitrated deposition surface area of 1.5 cm^2.

The deposited mass and thickness range of the processed coatings were studied under fixed electrokinetic parameters using different concentrated suspensions (1 g L^{-1}, 0.5 g L^{-1}, and 0.1 g L^{-1}). Fig. 3(a) displays the deposited PEI-GO mass at different times for each suspension. The suspensions with 1 g L^{-1} and 0.5 g L^{-1} concentrations were demonstrated to grow coatings with large masses (above 1 mg) and thicknesses (above 10 μm) for all the applied times, as shown in the inset FESEM

Open Access Article. Published on 21 August 2025. Downloaded on 3/5/2026 6:20:05 PM.
This article is licensed under a Creative Commons Attribution-NonCommercial 3.0 Unported Licence.

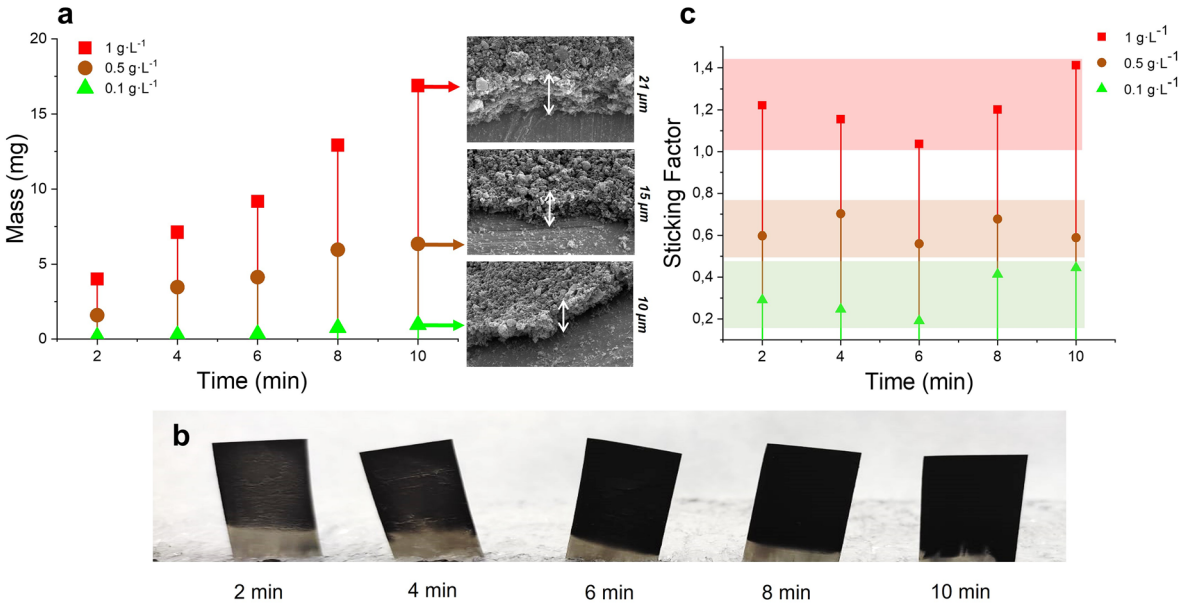

Fig. 3 (a) Deposited mass using different concentrated suspensions (1 g L^{-1}, 0.5 g L^{-1} and 0.1 g L^{-1}) keeping fixed EPD conditions. Inset: Cross-section SEM images of coatings prepared with different concentrated suspensions at 10 minutes. (b) Images of the coatings prepared with 0.1 g L^{-1} suspension for different deposition times. (c) Sticking factor (f) of the suspensions at different deposition times using a set current density of 53 μA cm^{-2}.

images. Although it is reported that the crystallographic structure of nickel favours the graphene oxide growth acting as nucleation points in a CVD synthesis,[35] in the electrically-driven GO deposition, binding energies are not that strong, and coatings above 0.26 mg cm^{-2} were not able to maintain being adhered to the Ni substrate.

Moreover, as Fig. 3(b) exhibits, the homogeneity of the coating is related to the deposition time, which must be greater than 4 minutes to obtain a homogeneous coating without superficial defects. Hence, reducing the thickness of the coating, while maintaining coating homogeneity is required.

Fig. 3(c) exhibits the sticking factor (f) of 3 different concentrated suspensions for different deposition times, calculated using eqn (1)–(3). The sticking factor represents the percentage of deposited/flocculated particles among those particles arriving at the working electrode by electrophoresis. The theoretical approach assumes that 100% of the particles that arrive on the electrode are deposited ($f = 1$).[32] The calculated sticking factor is above 1 for the 1 g L^{-1} suspension, ratifying the behaviour shown in the experimental kinetic curves (Fig. 3). When the quantity of suspended nanoplates is reduced, a considerable decrease in the sticking factor is shown, being $f \leq 0.8$ for 0.5 g L^{-1}. However, the most remarkable decrease in the sticking factor was seen for less concentrated PEI-GO suspension (0.1 g L^{-1}), minimizing the sticking factor by more than 60% in the whole deposition time range. Therefore, the potential to extend the deposition durations for the acquisition of thin, uniform coatings while sustaining a high current density of 53 μA cm^{-2} was facilitated through the reduction of PEI-GO loadings and the consequent diminishing of the suspension sticking factor. Thus, 0.1 g L^{-1} suspension was proven to meet all the requirements, reaching a homogeneous coating in 10 minutes with a maximum 10 μm thickness and a certain mass below 1 mg, avoiding layer detachment.

To understand the crystallographic properties of the commercial inorganic powder and its improvement during the deposition process, the crystallographic characterization of the commercial powder and the powder deposited were carried out. Fig. 4(a) shows the XRD pattern of the initial GO powder (GO red line) and the patterns of different coatings prepared using a 1 g L^{-1} suspension. The cathodic EPD was performed for 10 minutes at different current densities (53 μA cm^{-2}, 40 μA cm^{-2}, and 20 μA cm^{-2}) and, consequently, different electric fields were measured for each galvanostatic condition (56 V cm^{-1}, 40 V cm^{-1} and 23 V cm^{-1}). All the samples displayed a strong characteristic peak of graphitic atomic structures at 26.7°.

However, the (001) plane related to the expanded interlayer spacing caused by oxygen-containing functional groups was not observed in any spectrum. These phenomena may be caused by an intensive chemical or thermal exfoliation process during the synthesis of the commercial powder. Moreover, the coating prepared at the highest current density displays a small, wide diffraction peak at 20.5°, which was correlated with electrochemically reduced graphene oxide (ErGO).[36,37] At this current density of 53 μA cm^{-2}, a potential field of 56 V cm^{-1} is applied. Considering that the ErGO coating is not higher than 10 μm (for the 0.1 g L^{-1} suspension), the reduction potential applied during the electrophoretic deposition process to the GO layer is over 56 kV. Consequently, by the time the nanoplates deposit homogeneously on the substrate, oxygen-containing functional groups of the PEI-GO surface are reduced, restoring the sp^2 hybridization of the carbonaceous network. Thus, a relevant

Open Access Article. Published on 21 August 2025. Downloaded on 3/5/2026 6:20:05 PM.
This article is licensed under a Creative Commons Attribution-NonCommercial 3.0 Unported Licence.

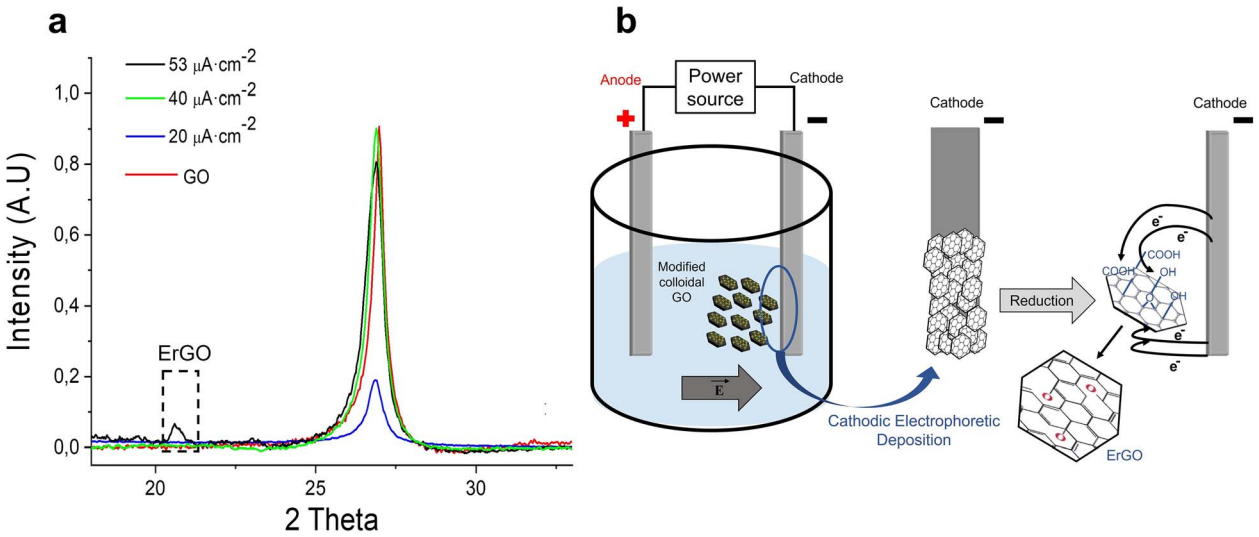

Fig. 4 (a) XRD patterns of 3 different coatings obtained by applying different current densities. (b) Cathodic electrophoretic deposition and the reduction process phenomena of the modified GO sheets in the cathode during the processing of the material.

improvement in the electrochemical properties of the material by a crystallographic modification during the material processing could be expected.

Fig. 4(b) displays a scheme of the electrochemical reduction process of PEI-GO at the cathode during the deposition of the coatings. When the electric field is applied, sp^3 hybridizations related to oxygen functional groups are eliminated through the reduction reactions displayed in Table 5. Through electrophoretic cathodic deposition, graphene oxide is deoxygenated, restoring the sp^2 hybridization, facilitating electron mobility, and improving the electrical conductivity of the material. The electrochemical reduction takes place just before the adhesion of GO on the metallic substrate. By the time the GO nanoplate is adhering to the cathodic nickel substrate, which, due to the applied electric field, is negatively charged with an excess of electrons, the carboxyl, hydrocarbon, or carbonyl functional groups of the graphene oxide surface are reduced. Nevertheless, the electronic network of GO could not be completely restored through electrochemical reduction due to the presence of vacancies on the atomic structure, which may decrease the electrochemical performance of the electrode.

As the atomic structural conformation of 2D materials cannot be deeply studied by X-ray diffraction analysis, Raman spectroscopy was used to evaluate the processing effect on the nanoplatelet electronic network. The Raman spectra of three coatings obtained using different concentrated suspensions and a fixed electric field of 56 V cm^{-1} were studied, as shown in Fig. 5. The spectra of the as-received GO and the different coatings revealed two dominant peaks of the G (1579–1565 cm^{-1}) and 2D band (2685–2700 cm^{-1}) that are assigned to graphite.

The weak D band (1328 cm^{-1}) caused by structural disorder was also observed. A considerable intensity increase of the 2D peak can be seen when the inorganic loading of the suspensions drops from 1 g L^{-1} to 0.5/0.1 g L^{-1}. Thus, a major 2D/G ratio value (from 0.84 to 0.96) is obtained between the highest and the lowest concentrated suspensions, as is shown in Table 6. The increased ratio translates into an improved dispersion and deagglomeration of GO, manifesting as decreased instances of graphene sheet stacking during the fabrication of coatings from low-concentration suspensions (0.5 and 0.1 g L^{-1}).

Moreover, by reducing the GO charge of the suspensions, we are able to avoid the coagulation and agglomeration of the particles to achieve a thinner-oriented few-layered GO coating.[38] Thus, this strategy could improve the adhesion of the material to the substrate, decreasing the number of stacked graphene nanoflakes and favoring its orientation during stacking.[39]

Contrary to the behaviour of the 2D peak, the D peak reduced its intensity and widened the peak for coatings prepared using suspensions with inorganic loadings below 1 g L^{-1}. The peak denoted as D is correlated to the atomic defects, and therefore, the electronic structure of the graphitic materials. Although no

Table 5 GO to ErGO: oxygen-containing functional groups and reduction reactions on the cathode

Carboxyl → Carbonyl	$\leftarrow R-\overset{\overset{O}{\|}}{C}-O + 2H^+ + 2e^- \rightarrow R-\overset{\overset{O}{\|}}{C}-H + H_2O$
Carbonyl → Hydroxycarbon	$\leftarrow R-\overset{\overset{O}{\|}}{C}-R' + 2H^+ + 2e^- \rightarrow R-\overset{\overset{O}{\|}}{C}-R'$
Hydroxycarbon → Hydrocarbon	$\leftarrow R-\overset{\overset{O}{\|}}{C}-R' + 2H^+ + 2e^- \rightarrow R-C-R' + H_2O$

Open Access Article. Published on 21 August 2025. Downloaded on 3/5/2026 6:20:05 PM.
This article is licensed under a Creative Commons Attribution-NonCommercial 3.0 Unported Licence.

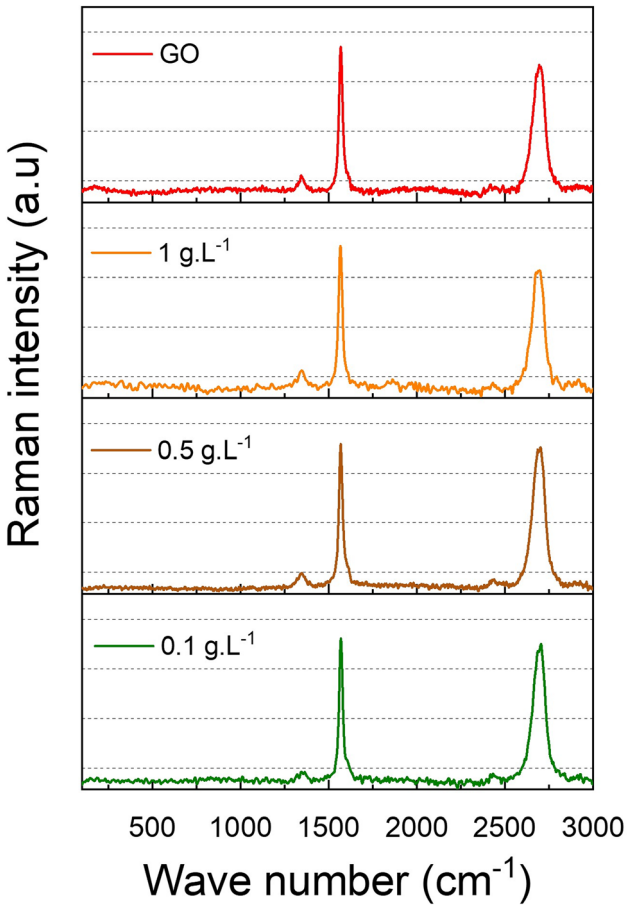

Fig. 5 Raman spectra of the as-received GO and the 3 coatings made by suspensions with different graphene oxide loads.

Table 6 Raman spectra (2D/G and D/G) and XPS (C/O) defect density ratio

	2D/G	D/G	C/O
GO	0.84	0.16	—
1 g L^{-1}	0.84	0.16	0.31
0.5 g L^{-1}	0.96	0.13	0.36
0.1 g L^{-1}	0.96	0.11	0.55

significant differences in the D/G ratio were observed for coatings prepared from the more concentrated suspension (1 g L^{-1}) and as-received GO, coatings derived from less concentrated suspensions (0.5 g L^{-1} and 0.1 g L^{-1}) exhibited a considerable reduction in this ratio. Specifically, a decrease of up to 25% was observed for the 0.1 g L^{-1} suspension (Table 6), indicating a lower amount of oxygen-containing sp^3 defects and a substantial restoration of the sp^2 carbon network. This improved atomic structural integrity is expected to enhance the electrochemical properties of the active material. The application of the same electric field to the less concentrated PEI-GO suspension during the cathodic EPD showed the successful reduction of the oxidized species, while the stacking is improved.

To confirm the reduction process through cathodic EPD at the surface level, the C 1s XPS spectra were deconvoluted and analyzed for coatings prepared with the highest (Fig. 6(a) and lowest (Fig. 6(b)) solid-content suspensions. The peak observed at 284.5 eV exhibits a slight augmentation in intensity with the decreasing loading of GO within the suspension. This phenomenon implies a substantial re-establishment of oxygen-containing sp^3 hybridization onto the sp^2 C–C bonds. The spectral peaks corresponding to oxygen functionalities, including the C–OH, C–O–C, C=O, and O–C=O bonds, are discernible at approximately 285.7, 286.8, 287.6, and 289.4 eV, respectively.[15,40] While the C–O–C and O–C=O peaks appear slightly above their typical ranges, such shifts can be attributed to overlapping peak contributions and local electronic environments in the ErGO network.[40] In the spectra obtained at a concentration of 0.1 g L^{-1}, a slightly broader peak associated with the C–OH binding and the appearance of a small O=C–OH peak is noted. However, alongside this, there is a discernible decrease in C–O–C and C=O functional groups. Moreover, Fig. 6(c) displays the O 1s region of coating surfaces manufactured using different concentrated suspensions. Significant intensity differences between the coatings fabricated with the highest and lowest PEI-GO content are visible. This disparity in peak intensities, alongside the C/O ratios (Table 6) and the results obtained in the C 1s region, may suggest a selective reduction at the surface of the oxygen-carbon species while slightly increasing the high hydrophilic carboxyl groups (–COOH) (see Fig. 6(d)), supporting the overall reduction process of the cathodic EPD fabrication process but also enhancing surface reactivity.[41]

Coatings with the same active mass were prepared using different nickel-based architectures to test the electrochemical performance of electrodes prepared by cathodic EPD. As

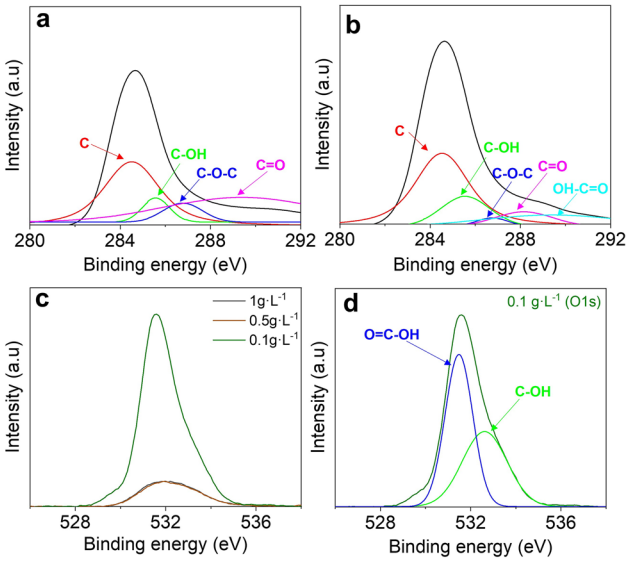

Fig. 6 C 1s XPS spectra for coatings fabricated by cathodic EPD using 1 g L^{-1} (a) and 0.1 g L^{-1} (b) suspensions. O 1s region of 3 coatings fabricated with different concentrated suspensions (c) and deconvoluted O 1s region of 0.1 g L^{-1} (d).

Open Access Article. Published on 21 August 2025. Downloaded on 3/5/2026 6:20:05 PM.
This article is licensed under a Creative Commons Attribution-NonCommercial 3.0 Unported Licence.

previously proved, a certain mass of 1 mg is the maximum quantity of material that can be deposited without overcoming the binding adhesion energies of the carbonaceous coating on the metallic nickel plates. Therefore, coatings of 0.5 mg were deposited on nickel substrates, both plates, and foams, using the previously set electrokinetic parameters (0.1 g L^{-1} suspension; 56 V cm^{-1}; 10 min). Prior to measuring their electrochemical response, all coatings were annealed at 350 °C for 1 h in an argon atmosphere to strengthen the carbonaceous microstructure and its adhesion to the metallic collector.

Fig. 7(a) shows the cyclic voltammetry curve at 50 mV s^{-1} of two substrates with the same coating load of the active material (≈0.5 mg) but different substrate architectures. The curves exhibit weak oxidation-reduction peaks of the metallic substrate at the highest and lowest voltages, respectively, being more evident for the plate-like substrate due to the lower electrochemical contribution of the ErGO coating.[42] A significant enlargement of the area under the curve and, consequently, an increase of stored charge is visible along the entire potential window on the coated foam substrate. Even though the two electrodes have the same quantity of the active material, the coating on the porous structure of the nickel foam seems to encourage a larger active specific area with a greater formation of the EDL. Fig. 7(b) exhibits the cyclic voltammetry curves of foam electrodes at different scan rates from 50 mV s^{-1} to 2 mV s^{-1}. At the lowest scan rates, the redox peaks of the substrate are more noticeable; however, the irreversibility of the substrate redox reaction minimizes its contribution at the highest scan rates.

Fig. 7(c) exhibits the microstructure of the coatings on both the nickel plate and foam. Both images reveal a massive deposition with uncovered zones on the substrate surface, which account for the redox contribution of the substrate. Nevertheless, clear differences in morphology and coverage are evident. On the plate, the coating appears continuous but dense, with visible cracking likely caused by internal stresses during deposition or drying. In contrast, the coating on the 3D nickel foam conforms closely to the porous scaffold, creating a finer and more open texture that facilitates ion accessibility.

The more porous microstructural configuration on the foam substrate is favourable for electrochemical double-layer (EDL) formation, as it increases the exposure of active sites for K^+ and OH^- ion adsorption. Moreover, the uniform covering on the macrostructural porous architecture supports better electrolyte penetration and promotes a higher electrochemically active surface area (ECSA), which directly contributes to improved capacitive behavior. The thinner, more uniform coating on the foam also demonstrates better adhesion, consistent with

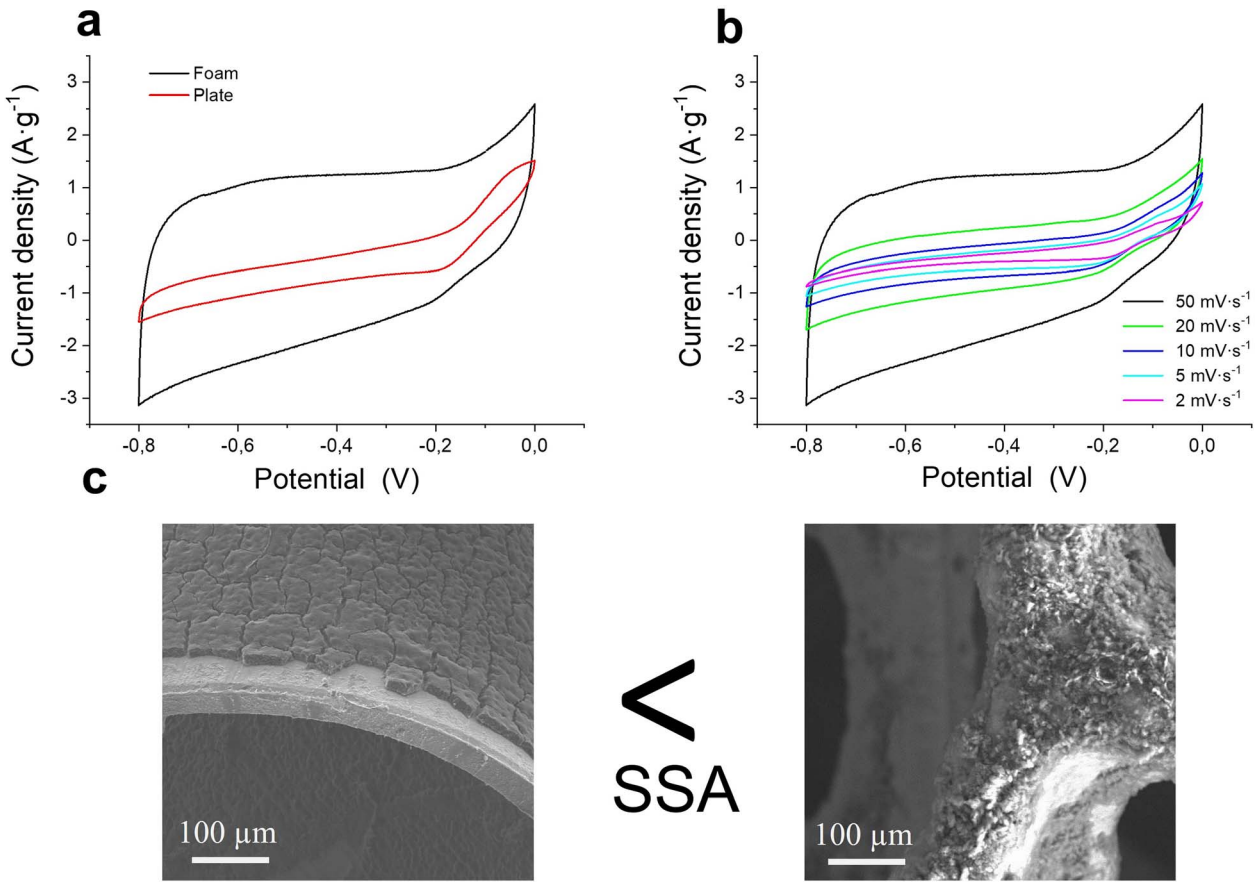

Fig. 7 (a) Cyclic voltammetry curves at a scan rate of 50 mV s^{-1} of the plate and foam depositions. (b) Cyclic voltammetry curves of foam reduced graphene oxide coating at scan rates of 50, 20, 10, 5, and 2 mV s^{-1}. (c) SEM images of ErGO coatings on plate and foam metallic nickel substrates.

Open Access Article. Published on 21 August 2025. Downloaded on 3/5/2026 6:20:05 PM.
This article is licensed under a Creative Commons Attribution-NonCommercial 3.0 Unported Licence.

previous observations that electrically driven coatings with mass loadings above 0.26 mg cm^{-2} tend to delaminate from flat nickel substrates due to limited binding strength.[35] Although both electrode configurations exhibit homogeneous thickness due to the optimized cathodic EPD process, the plate substrates with smaller accessible deposition areas promote the growth of thicker ErGO coatings (up to 10 μm for 10 minutes depositions using 0.1 g L^{-1} suspensions; see Fig. 3(a)). The thicker coatings result in a reduced exposure of the active material and increased mechanical instability. In contrast, the foam substrates support much thinner coatings (below 5 μm) with minor GO layer stacking, as shown in the 2D/G ratio (Table 6). Thus, the enhanced mechanical interlocking, stability, and structure facilitate the partial restoration of the sp^2 carbon network, further contributing to superior electrochemical performance.

The capacitive performance for both configurations was tested by analysing galvanostatic charge–discharge curves (GCD) at different current densities. Fig. 8(a) exhibits the GCD triangular curves, which are related to the capacitive phenomenon. The slight lack of symmetry, more visible at lower current densities, can be attributed to minor faradaic contributions from residual oxygen-containing functional groups or the slightly exposed nickel substrate.[43] Nevertheless, the absence of voltage plateaus and the overall linearity of the profiles confirm a predominantly capacitive mechanism. At higher current densities, the curves become more symmetric, further supporting this conclusion. Additionally, the foam-based electrodes exhibit longer charge–discharge times, consistent with their larger electroactive surface area and enhanced EDL formation, as also evidenced by CV analysis.

Gravimetric specific capacitance (C_S) values for different current densities, calculated using eqn (4), are summarized in Fig. 8(b). The foam electrode shows an increase in specific capacitance, in comparison with the plate electrode, for all the current density range. The difference in gravimetric specific capacitance at lower current densities, as the charge–discharge times, is significantly higher than at high current density values. This is largely due to the increase in the reaction time as the applied current density decreases, favouring, again, the pseudocapacitive contribution of the oxygen-containing functional groups and the redox contribution of the substrate, more visible in foam electrodes, reaching 148 F g^{-1} at 1.5 A g^{-1}. Nevertheless,

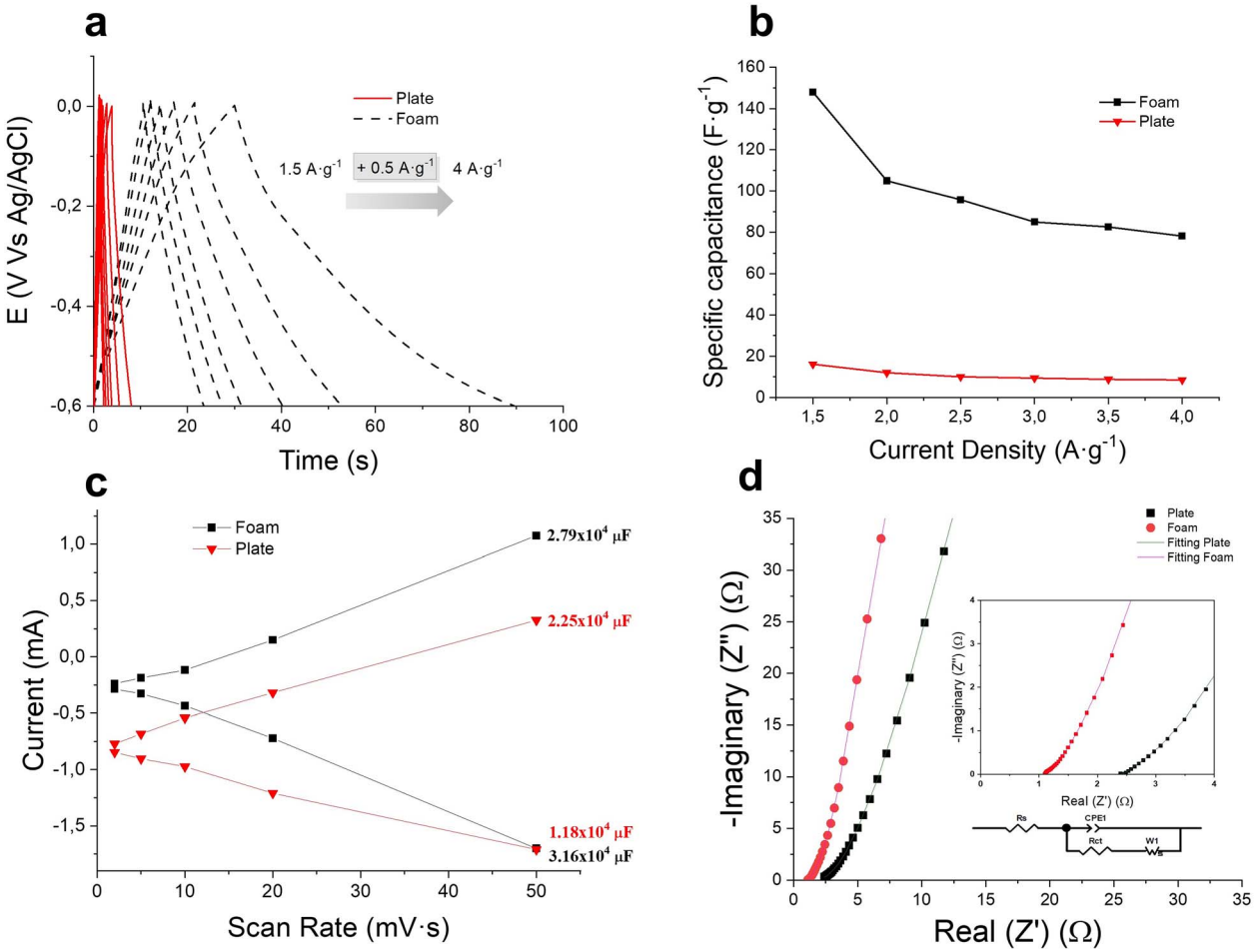

Fig. 8 (a) GCD at different current densities of ErGO coatings on a Ni plate and foam measured between −0.6 to 0 V potential *vs.* Ag/AgCl. (b) Specific gravimetric capacitance at different current densities of plate and foam coatings. (c) Anodic and cathodic currents of foam and plate coatings measured between −0.6 to 0 V potential *vs.* Ag/AgCl. Inset: calculated double-layer capacitance values (C_{DL}). (d) EIS plots of GO coatings on nickel plate and foam substrates and the corresponding fitted curves. Inset: equivalent circuit.

Open Access Article. Published on 21 August 2025. Downloaded on 3/5/2026 6:20:05 PM. This article is licensed under a Creative Commons Attribution-NonCommercial 3.0 Unported Licence.

the superiority of the foam electrode is visible for all current density rates from 2 A g^{-1} to 4 A g^{-1}, where the capacity is increased by 90% compared to the plate electrode. Moreover, the capacitive ErGO coating in the foam substrate achieves 80 F g^{-1} at a high-current density of 4 A g^{-1}, exhibiting excellent supercapacitor behaviour in fast charge–discharge processes.

The manufactured ErGO electrodes utilizing cathodic EPD over nickel foams displayed slightly lower specific capacitance values than the electrodes developed by Srinivas Gadipelli *et al.*[8] by directly pressing dry powders over nickel foams (Table 1). Under identical electrochemical testing conditions, a specific capacitance of over 220 F g^{-1} at a current density of 2 A g^{-1} was achieved by the pressed rGO electrodes, compared to the 104 F g^{-1} achieved in this work. Nonetheless, the conventional, non-scalable, and less sustainable thermal and pressing strategies used in that approach limit its broader applicability when compared to the simultaneous cathodic EPD reduction and shaping strategy applied here.

Moreover, the cathodic EPD process yielded ErGO electrodes with enhanced performance, surpassing the specific capacitance values reported by Purkait *et al.*[10] and Yang *et al.*[11] The electrodes fabricated using electrical deposition shaping techniques attained specific capacitances of 40.0 and 99.8 F g^{-1} at current densities of 2 A g^{-1}, which are approximately half and slightly below the 105 F g^{-1} achieved by the developed ErGO electrodes under the equivalent current densities in this study. However, both works used non-aqueous polymer-based electrolytes in electrochemical measurements. Other investigations presented in Table 1 demonstrated that electrodes deposited *via* dip coating and subsequently electrochemically reduced, as conducted by Wanli *et al.*,[9] achieved slightly elevated specific capacitances of 160.8 F g^{-1} compared to the present. However, these results were obtained under potentiostatic conditions at low scan rates of 10 mV s^{-1}.

When compared to electrodes manufactured and tested under similar conditions (1.5 mA cm^{-2} and 1 M Na_2SO_4), the electrically deposited and electrochemically reduced electrodes developed by Xuejun *et al.*[12] exhibited lower capacitance values of 110.0 F g^{-1}. Conversely, Wang *et al.*[12] obtained a slightly higher capacitance of 172 F g^{-1} using a chemically reduced electrode. However, the value was obtained at a lower current density of 0.2 A g^{-1}, indicating a comparable performance to the present study. Zisong *et al.* and Baozhen *et al.*[12] achieved superior specific capacitance values of 167.0 F g^{-1} and 190.0 F g^{-1}, respectively, at low current densities of 0.5 A g^{-1}, using acidic (0.5 M H_2SO_4) and more concentrated KOH (6 M) electrolytes. Under the same gravimetric conditions as the present study (2 A g^{-1}), they maintained higher specific capacitances of approximately 110.0 F g^{-1} (chemically reduced) and 130.0 F g^{-1} (electrochemically reduced), compared to the 99.8 F g^{-1} reported here. However, in both cases, acids and highly concentrated salts were used during the reduction of GO coatings and electrochemical measurements, respectively, which may influence the performance and limit the sustainability, efficiency, and scalability of the processes.

To analyze the improvement in capacitive performance, a more in-depth study of the EDL was performed. Current values from the cathodic and anodic curves at a potential of 0.5 V were plotted against various scan rates from the CV, as shown in Fig. 8(c). The different scan rates and current values resulted in a linear fit ($\chi^2 \sim 10^{-1}$), where the slope of the fitting corresponds to the CDL as defined in eqn (7). Although the plate coatings exhibit considerably higher current values at low scan rates, the foam coating current increases noticeably at high scan rates, displaying a more pronounced slope in both the anodic and cathodic curves. The fitting obtained from these current values and scan rates demonstrates a larger double-layer formation in the foam electrode.

Using the CDL values subtracted from the linear fitting and the theoretical CTS of single-layer graphene oxide (21 μF cm^{-2}), the ECSA was calculated (eqn (5)) and is presented in Table 7. The use of colloidal processing and cathodic EPD, in addition to improving the electronic properties of the material, enables covering the internal segments of the porous structures during deposition, enhancing the electrochemical performance of the active material by increasing the ECSA. The improvement in the active material percentage was calculated by comparing the ECSA with the deposited BET area using eqn (8) and (9). Thus, the electrochemical response of the same deposited material quantity was improved by 20% with the fixed parameters when a nickel foam is used as substrate.

The electrochemical behaviour of both graphene oxide coatings was further studied through electrochemical impedance spectroscopy (EIS). Nyquist plots in Fig. 8(d) display the curves of ErGO coatings on nickel plates and foams. The respective fitted impedance diagrams obtained through the equivalent circuit using 'ZView' software are shown as an inset in the same figure. The combined resistance (RS) of the active material, ionic resistance of the electrolyte, and interphase resistance of the electrode/substrate corresponds to the value where the curve intercepts the real axis, at high frequencies. Additionally, the radius of the semicircle was calculated, together with the electrode conductivity and charge transfer resistance (R_{CT}) of the bulk electroactive material (Table 8).

Table 7 Electrochemical properties of the coated electrodes

Coating substrate	Foam	Plate
Average capacitance $C_{DL} \times 10^4$ (μF)	2.90	2.03
ECSA (cm^2)	1382	968
Deposited BET area (cm^2)	2408	2697
Active material (%)	57	37

Table 8 Comparison of the fitted EIS parameters of ErGO electrodes with different substrates[a]

Sample	R_s (Ω)	R_{CT} (Ω)	CPE-P
Plate	2.47	1.21	0.85
Foam pre-cycling	1.17	0.47	0.89
Foam post-cycling	1.76	0.51	0.84

[a] All the EIS fitted data exhibit error values of $\chi^2 \sim 10^{-2}$.

Open Access Article. Published on 21 August 2025. Downloaded on 3/5/2026 6:20:05 PM.
This article is licensed under a Creative Commons Attribution-NonCommercial 3.0 Unported Licence.

They showed slightly different behaviours in terms of the electrode/substrate interphase and charge transfer resistance. Equivalent circuits that were used to fit the impedance diagrams are shown as an inset in the same figure. EIS Nyquist plots show different combined resistance values of ErGO coatings depending on the architecture on nickel substrates, exhibiting larger R_S for the plate configuration electrode (2.47 Ω) compared with the foam electrode (1.17 Ω). Furthermore, charge transfer resistance also shows a similar behaviour, being considerably lower in the nickel foam (0.47 Ω) compared to the plate coating R_{CT} (1.21 Ω). This performance is correlated to the nanoflake configuration and the microstructure of the coating on the substrate. Increasing the substrate area improved the interphase between the deposited active material and the metallic substrate. Thus, the improved orientation of ErGO nanoflakes and the decreasing coating thickness led to a minor charge transfer resistance.

Previously described serial resistance appears in series with a constant phase element (CPE) that represents the combination of surface modification capacitance and double layer formation capacitance, which simulates the non-ideal behaviour of the capacitor. Both coated plate and foam electrodes display similar CPE-P values of 0.85 and 0.89, respectively. The finely adjusted ErGO electrodes acquired through cathodic EPD demonstrated interfacial properties analogous to those of ErGO/NiO electrodes prepared *via* the same technique, where complete coverage by the chemically reduced graphene on the NiO nanoplate surfaces was proven, validating the ErGO processing.[44]

The results of CV, GCD, specific capacitance, and impedance spectroscopy analysis suggested a larger formation of the EDL in the case of coated foams. The higher ECSA (1382 cm^2) and the lower charge transfer resistance (R_{CT} = 0.47 Ω), certify the enhanced electrochemical performance of the ErGO coating (of 0.5 mg of electroactive material) of the foam substrate, while the selective reduction of GO nanoflakes taking place simultaneously to the EPD, verified by the XPS results and an R_s of 1.17 Ω, evidences a larger contact area between the active material and the electrolyte. Thus, cycling stability (black dots) and capacitance retention (green dots) of coated foam electrodes were tested at different current densities and 2 A g^{-1}, respectively (Fig. 9(a)). A 35% capacitance loss is observed in the first 400–500 cycles, with the most pronounced decrease occurring during the initial 200 cycles (at 2 A g^{-1}), coinciding with the lowest applied current density of 1.5 A g^{-1} at the cycling stability (black dots) curve. This behavior can be attributed to an electrochemical activation process, as recently described by Bernicola *et al.*[45] in their study on nanoporous rGO electrodes. During the early stages of cycling, a significant evolution in voltammetric response and specific capacitance occurs, which is attributed to the progressive infiltration of the electrolyte into

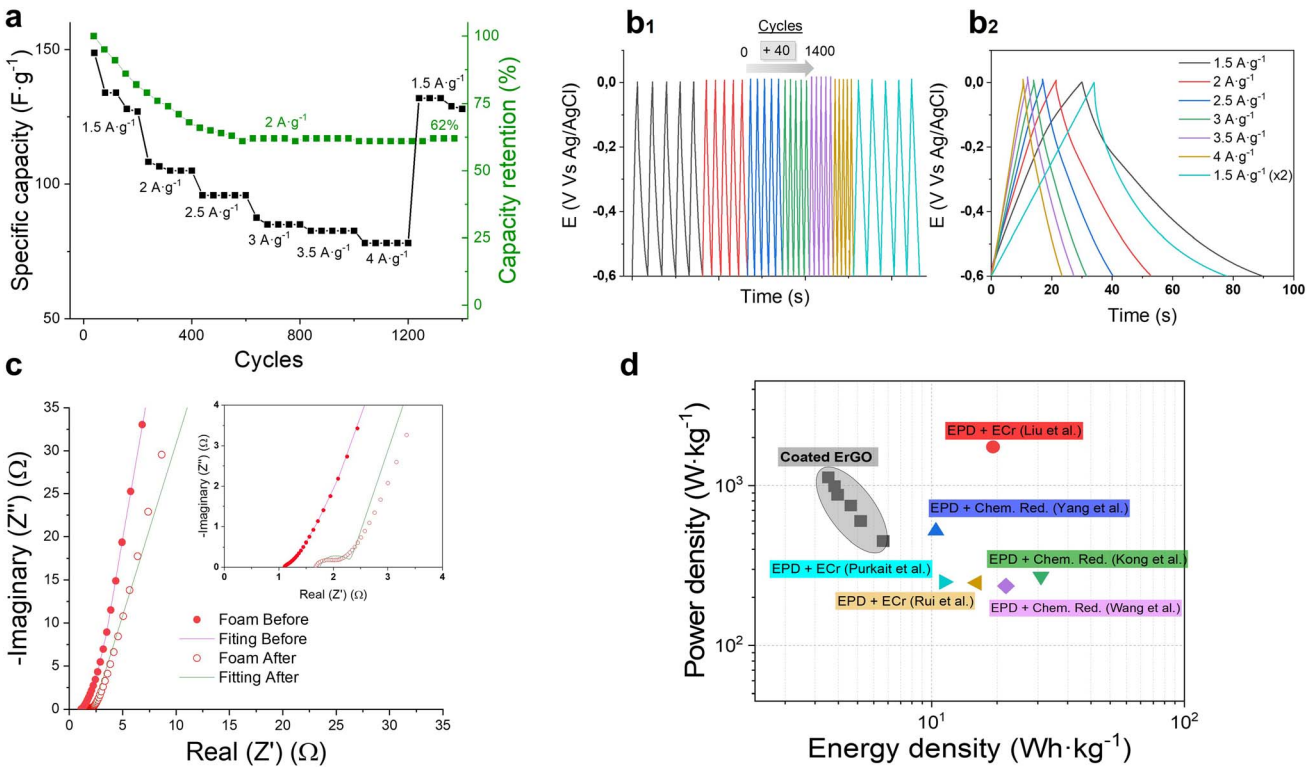

Fig. 9 (a) GCD cycling: capacitance evolution at different current densities and capacity retention at 2 A g^{-1}. (b_1) Set of 35 GCD curves, extracted from cycles 40 to 1400 in increments of 40 cycles, recorded at varying current densities during the cycling test of the symmetric full cell. (b_2) Detailed view of the GCD curves at different current densities. (c) EIS plots and fitted curves using the equivalent circuit of Fig. 8(d) of foam electrodes before and after GCD cycling. (d) Ragone-plot comparison of the developed electrode at different current densities with the rGO-based electrodes of Table 1.

Open Access Article. Published on 21 August 2025. Downloaded on 3/5/2026 6:20:05 PM. This article is licensed under a Creative Commons Attribution-NonCommercial 3.0 Unported Licence.

the porous network and the activation of redox-active oxygen-containing functional groups.

In the present study, a similar activation mechanism may be occurring in the foam electrode, where the electrode configuration and coating chemistry evolve during initial cycling. The combination of early structural adjustments within the porous coating, partial irreversible reduction of previously not reduced oxygen functional groups,[46] and limited electrolyte accessibility at lower current densities (1.5–2 A g^{-1}) leads to a decrease in the specific capacitance at initial cycles. However, after this activation phase, the gravimetric specific capacitance remains stable for other current densities during the cycling test and suggests that the observed early-stage decay does not reflect permanent degradation but rather a dynamic adaptation of the electrode–electrolyte interface toward optimal performance. Thus, the electrochemical stability was demonstrated by reaching 90% of the capacitance (132 F g^{-1}) for 1.5 A g^{-1} after 1400 cycles.

Additionally, to further investigate the rate capability and charge storage mechanism of the symmetric full cells, the evolution of the GCD curves throughout the cycling test was analyzed. Fig. 9(b_1) presents a set of 35 GCD curves recorded between cycles 40 and 1400 at varying current densities. These curves display the characteristic triangular shapes typical of capacitive behavior, with slight asymmetries that are more noticeable at lower current densities, suggesting enhanced pseudocapacitive and faradaic contributions under these conditions. This behavior aligns with the trends observed in the previously discussed half-cell CV measurements and the capacitance results obtained in the symmetric full-cell configuration. Furthermore, Fig. 9(b_2) provides a closer view of the GCD curves at different current densities, revealing that the asymmetry becomes slightly less pronounced in the later cycles at lower current densities. This observation supports the occurrence of an initial activation process, related to the presence of residual oxygen-containing functional groups and possible substrate effects, and the progressive stabilization of the electrode surface during long-term cycling.

The stabilization of the capacitance observed after prolonged cycling was further supported by EIS analysis (Fig. 9(c)). The post-cycling Nyquist plot of the same foam-based electrode reveals the constancy of the electrochemical performance, suggesting microstructural and compositional stabilization. While the R_s (1.76 Ω) shows a slight increase, likely due to minor degradation or electrolyte modifications, the R_{CT} remains close to the pre-cycling values (0.47–0.51 Ω). The small fluctuations corroborate the uniform and stabilized interface between the electroactive coating and the underlying nickel architecture after the cycling test. Furthermore, the maintained CPE value (0.84) and small deviation in the phase exponent confirm the capacitive response. This deviation likely reflects the appearance of additional interfacial processes rather than significant structural or compositional degradation. Instead, the consistent electrochemical performance observed after the initial cycles, together with the stabilized capacitance and stabilized charge transfer characteristics, suggests that the electrode maintains its structural and compositional integrity after prolonged cycling, with only minor interfacial reconfigurations influencing ionic and electronic transport.

Fig. 9(d) displays the performance of a symmetric full-cell under different current densities evaluated in terms of energy/power densities calculated by applying eqn (10) and (11). Regarding the power densities, a rapid charge/discharge was probed for the manufactured coated ErGO foam electrodes, ranging from 400–1125 W kg^{-1}. The coated ErGO electrodes exhibited power densities that were comparable to, and in some cases exceeded, those of rGO-based and ErGO-based EDLCs tested under similar conditions reported in Fig. 9(c), while consistently maintaining energy capacitances in the medium range of $\sim 10^1$ Wh kg^{-1}. These values were obtained across a range of current densities (1.5 A g^{-1} to 4 A g^{-1}), highlighting the stable and reliable electrochemical performance of the electrodes under varying operational conditions. Thus, promising competitive coated ErGO supercapacitors for a broad range of applications were developed using a straightforward, scalable, and sustainable reduction and manufacturing process.

Conclusions

Colloidal dispersion and stabilization of the modified PEI-GO and optimization of the electrokinetic parameters of the suspension enable cathodic EPD and the simultaneous selective electrochemical reduction of nanoflakes to obtain strongly active and adhered homogeneous thin coatings of ErGO for high-performance supercapacitor electrodes. By tuning the electrical parameters and suspension concentrations, the proposed process enables the optimization of electrochemical and electrical properties of PEI-GO coatings by decreasing oxygen-carbon functional groups of the GO surface, maintaining the reactive hydroxyl-containing sites, which could be the cause of the achieved high-capacity values (148 F g^{-1}) and high-capacity retention (100%) at 1.5 A g^{-1}.

Thin and compact ErGO coatings were formed *via* electron transfer between the working metallic substrate and the surface of the deposited material. This process induces a reduction in atomic structural defects of graphene in the form of sp^3 hybridization, as suggested by crystallographic characterization.

Moreover, the coagulation of PEI-GO nanoflakes during cathodic EPD led to a high electrochemical performance of the active microstructure and a complete covering of 3D complex metallic substrates, improving the formation of EDL. The ECSA estimation highlighted the empowerment of the active material and efficiency of the processing and shaping method, upgrading the percentage of the exposed active material by 20%. The developed device displayed rapid charge/discharge processes, achieving 80 F g^{-1} capacitance at a high current density (4 A g^{-1}), and therefore, a competitive power density of 10^3 W Kg^{-1}. Consequently, a binder-free high-performance supercapacitor was produced through a sustainable and scalable manufacturing process exhibiting significant power density and moderate energy density comparable to conventional EDLCs.

 This journal is © The Royal Society of Chemistry 2025

Open Access Article. Published on 21 August 2025. Downloaded on 3/5/2026 6:20:05 PM. This article is licensed under a Creative Commons Attribution-NonCommercial 3.0 Unported Licence.

Conflicts of interest

There are no conflicts to declare.

Data availability

The data are available from the corresponding author on reasonable request.

Supplementary information is available. See DOI: https://doi.org/10.1039/d5ta00888c.

Acknowledgements

This work was supported by the grant PID2022-137274NB-C31/ funded by MICIU/AEI/10.13039/501100011033 and ERDF/EU and the grant TED2021-129920B–C41 funded by MICIU/AEI/ 10.13039/501100011033 and the European Union NextGenerationEU/PRTR".

References

1 F. J. de Sisternes, J. D. Jenkins and A. Botterud, *Appl. Energy*, 2016, **175**, 368–379.
2 N. Kumar, S. Bin Kim, S. Y. Lee and S. J. Park, *Nanomaterials*, 2022, **12**, 3708.
3 S. Kondrat, C. R. Pérez, V. Presser, Y. Gogotsi and A. A. Kornyshev, *Energy Environ. Sci.*, 2012, **5**, 6474–6479.
4 L. Fekri Aval, M. Ghoranneviss and G. Behzadi Pour, *Heliyon*, 2018, **4**, 862.
5 S. Singh, M. R. Hasan, P. Sharma and J. Narang, *KeAi Communications Co*, 2022, **3**, 100190.
6 J. Xu and D. Zhang, *Electrochim. Acta*, 2017, **224**, 105–112.
7 K. S. Novoselov, A. K. Geim, S. V Morozov, D. Jiang, Y. Zhang, S. V Dubonos, I. V Grigorieva and A. A. Firsov, *Science*, 2004, **306**, 666–669.
8 S. Gadipelli, J. Guo, Z. Li, C. A. Howard, Y. Liang, H. Zhang, P. R. Shearing, D. J. L. Brett, S. Gadipelli, J. Guo, Y. Liang, H. Zhang, P. R. Shearing, D. J. L. Brett, Z. Li and C. A. Howard, *Small Methods*, 2023, **7**, 2201557.
9 W. Gao, C. Debiemme-Chouvy, M. Lahcini, H. Perrot and O. Sel, *Anal. Chem.*, 2019, **91**, 2885–2893.
10 T. Purkait, G. Singh, D. Kumar, M. Singh and R. S. Dey, *Sci. Rep.*, 2018, **8**, 640.
11 J. Yang, W. Weng, Y. Zhang, X. Du, Y. Liang, L. Yang, X. Luo, Y. Cheng and M. Zhu, *Carbon*, 2018, **126**, 419–425.
12 X. Liu, X. Qi, Z. Zhang, L. Ren, G. Hao, Y. Liu, Y. Wang, K. Huang, X. Wei, J. Li, Z. Huang and J. Zhong, *RSC Adv.*, 2014, **4**, 13673–13679.
13 M. Wang, L. D. Duong, N. T. Mai, S. Kim, Y. Kim, H. Seo, Y. C. Kim, W. Jang, Y. Lee, J. Suhr and J. Do Nam, *ACS Appl. Mater. Interfaces*, 2015, **7**, 1348–1354.
14 Z. Kong, Y. Gao, X. Ma, Q. Gou, Z. Yan, W. Huang, H. Tan, X. Cai and J. Cai, *Int. J. Electrochem. Sci.*, 2018, **18**, 11.
15 B. Rui, M. Yang, L. Zhang, Y. Jia, Y. Shi, R. Histed, Y. Liao, J. Xie, F. Lei and L. Fan, *J. Appl. Electrochem.*, 2020, **50**, 407–420.
16 M. P. Lavin-Lopez, A. Paton-Carrero, L. Sanchez-Silva, J. L. Valverde and A. Romero, *Adv. Powder Technol.*, 2017, **28**, 3195–3203.
17 N. Sharma, S. Tomar, M. Shkir, R. Kant Choubey and A. Singh, in *Materials Today: Proceedings*, 2019, vol. 36, pp. 730–735.
18 L. Dong, J. Yang, M. Chhowalla and K. P. Loh, *Chem. Soc. Rev.*, 2017, **46**, 7306–7316.
19 M. Brycht, A. Leniart, J. Zavašnik, A. Nosal-Wiercińska, K. Wasiński, P. Półrolniczak, S. Skrzypek and K. Kalcher, *Anal. Chim. Acta*, 2018, **1035**, 22–31.
20 Z. Fan, K. Wang, T. Wei, J. Yan, L. Song and B. Shao, *Carbon*, 2010, **48**, 1686–1689.
21 X. Díez-Betriu, F. J. Mompeán, C. Munuera, J. Rubio-Zuazo, R. Menéndez, G. R. Castro and A. De Andrés, *Carbon*, 2014, **80**, 40–49.
22 A. Zhou, J. Bai, W. Hong and H. Bai, *Carbon*, 2022, **191**, 301–332.
23 J. Jiang, X. Yao, C. Xu, Y. Su, C. Deng, F. Liu and J. Wu, *J. Electrochem. Soc.*, 2016, **163**, 133–139.
24 P. Collini, S. Kota, A. D. Dillon, M. W. Barsoum and A. T. Fafarman, *J. Electrochem. Soc.*, 2017, **164**, D573–D580.
25 Y. Ma, J. Han, M. Wang, X. Chen and S. Jia, *J. Chin. Ceram. Soc.*, 2018, **4**, 108–120.
26 M. Diba, D. W. H. Fam, A. R. Boccaccini and M. S. P. Shaffer, *Prog Mater Sci.*, 2016, **82**, 83–117.
27 J. Jiang, X. Yao, C. Xu, Y. Su, C. Deng, F. Liu and J. Wu, *J. Electrochem. Soc.*, 2016, **163**, 133–139.
28 M. Mallick and A. N, *Surf. Coat. Technol.*, 2022, **450**, 128946.
29 H. Purwaningsih, N. M. I. P. Suari, W. Widiyastuti and H. Setyawan, *ACS Omega*, 2022, **7**, 6760–6767.
30 O. Urra Sanchez, H. Besharatloo, J. Yus, A. J. Sanchez-Herencia and B. Ferrari, *Addit. Manuf.*, 2023, **72**, 103643.
31 Z. Gonzalez, J. Yus, A. Caballero, J. Morales, A. J. Sanchez-Herencia and B. Ferrari, *Electrochim. Acta*, 2017, **247**, 333–343.
32 P. Sarkar and P. S. Nicholson, *JACS*, 1996, **79**, 1987–2002.
33 P. Connor, J. Schuch, B. Kaiser and W. Jaegermann, *Z. fur Phys. Chem.*, 2020, **234**, 979–994.
34 J. Xia, F. Chen, J. Li and N. Tao, *Nat. Nanotechnol.*, 2009, **4**, 505–509.
35 J. Zheng, Y. Wang, L. Wang, R. Quhe, Z. Ni, W. N. Mei, Z. Gao, D. Yu, J. Shi and J. Lu, *Sci. Rep.*, 2013, **3**, 2081.
36 L. Stobinski, B. Lesiak, A. Malolepszy, M. Mazurkiewicz, B. Mierzwa, J. Zemek, P. Jiricek and I. Bieloshapka, *J. Electron Spectrosc. Relat. Phenom.*, 2014, **195**, 145–154.
37 S. K. Bikkarolla, P. Cumpson, P. Joseph and P. Papakonstantinou, *Faraday Discuss.*, 2014, **173**, 415–428.
38 M. Verde, M. Peiteado, A. C. Caballero, M. Villegas and B. Ferrari, *J. Colloid Interface Sci.*, 2012, **373**, 27–33.
39 A. Das, B. Chakraborty and A. K. Sood, *Bull. Mater. Sci.*, 2018, **31**, 579–584.
40 L. Shen, L. Zhang, K. Wang, L. Miao, Q. Lan, K. Jiang, H. Lu, M. Li, Y. Li, B. Shen and W. Zheng, *RSC Adv.*, 2018, **8**, 17209–17217.
41 H. J. Lee, J. S. Kim, K. Y. Lee, K. H. Park, J. S. Bae, M. Mubarak and H. Lee, *Sci. Rep.*, 2019, **9**, 557.

Open Access Article. Published on 21 August 2025. Downloaded on 3/5/2026 6:20:05 PM.
This article is licensed under a Creative Commons Attribution-NonCommercial 3.0 Unported Licence.

42 D. S. Hall, C. Bock and B. R. MacDougall, *J. Electrochem. Soc.*, 2013, **160**, 235–243.
43 P. Simon and Y. Gogotsi, *Nat. Mater.*, 2008, **7**, 845–854.
44 J. Yus, Y. Bravo, A. J. Sanchez-Herencia, B. Ferrari and Z. Gonzalez, *Electrochim. Acta*, 2019, **308**, 363–372.
45 M. del P. Bernicola, M. Lounasvuori, J. Padilla-Pantoja, J. Santiso, C. Debiemme-Chouvy, H. Perrot, T. Petit, J. A. Garrido and E. del Corro, *Adv. Funct. Mater.*, 2024, **34**, 2408441.
46 Y. J. Oh, J. J. Yoo, Y. Il Kim, J. K. Yoon, H. N. Yoon, J. H. Kim and S. Bin Park, *Electrochim. Acta*, 2014, **116**, 118–128.

 This journal is © The Royal Society of Chemistry 2025